The Pennsylvania State University

Electrical Engineering Department

University Park, Pennsylvania 16802

THEORY AND TESTS OF A THERMAL ION DETECTOR SENSITIVE ONLY AT NEAR-NORMAL INCIDENCE

(NASA-CR-164378) THEORY AND TESTS OF A THERMAL ION DETECTOR SENSITIVE ONLY AT NEAR-NORMAL INCIDENCE (Pennsylvania State Univ.) 55 p HC A04/MF A01 CSCL 14B
N81-25353
Unclas
G3/35 26506

National Aeronautics and Space Administration

Grant NSG-3166

James W. Robinson

June 1981

ABSTRACT

Measurements of thermal ions are influenced by factors such as spacecraft potential, velocity, angle of attack, and sheath size. A theory is presented for the response of an instrument which accepts ions only within a small angle of incidence from normal. Although a more general theory is available and forms the basis of this one, the small-angle restriction allows a simpler formulation which does not depend on sheath size. Furthermore, practical instruments are easily designed around this restriction. Laboratory tests verify that such instruments respond as expected and they illustrate how design details influence perturbations from the ideal response characteristics.

TABLE OF CONTENTS

LIST OF TABLES

LIST OF FIGURES

SYMBOL TABLE

A	Orifice Area
A_i	Coefficients Used for Evaluating J_x
A', A''	Effective Areas
a	$B\sqrt{W/2}$
B	$2M \cos \gamma$
b	$a^2 - V_s/W$
C	$S(\tan\alpha_o)/2$
D	Two Uses: $2M \sin \gamma$, Aperture Diameter
E	Normalized Particle Energy $V_s + X + Z$
F	Orifice Efficiency Parameter
G	Lower Limit of Z-Integration
H	Convenient Variable of Integration
I_o	Modified Bessel Function
I	Measured Current
I_i	Integrals Used for Evaluating J
J_o	Random Current Density $ne\sqrt{kT/2\pi m}$
J_i	Linear Combinations of I_i's
J_x	Factor of J
J	Normalized Current Density
L	λ/R
M	Mach Number $\lvert U_o \rvert \sqrt{m/2kT}$
n	Ion Density
R	Radius of Spacecraft

S	Aperture Separation
T	Two Uses: Ion Temperature, The Parameter $\sqrt{X/UZ}$
U	Maximum Allowed Ratio X/Z
V	Largest of 0, V_g, $-V_s$
U_o	Velocity of Spacecraft
V_s	Normalized Potential $V_s = v_s/V_T$
v_s	Potential of Spacecraft Relative to Plasma
V_g	Normalized Potential $V_g = v_g/V_T$
v_g	Potential of Repeller Grid or Drift tube Relative to Spacecraft
V_T	Normalizing Factor for Potentials $V_T = kT/e$
W	$1 + U$
X	Ion Kinetic Energy (Normalized by kT) Associated with The Tangential Velocity Component As Measured at The Orifice
Z	Same as X Except for Normal Velocity
α_o	Angle of Incidence at the Orifice $\tan \alpha_o = \sqrt{X/Z}$
α_∞	Angle of Incidence of Unperturbed Ion Trajectory
β	arcccos(2C/D)
γ	Mach Angle
λ	Debye Length or Approximate Sheath Thickness

INTRODUCTION

In this report is proposed a design for a spacecraft instrument which detects charged particles. Its function is like that of a Faraday cup yet its design alleviates many of the problems associated with Faraday cups. The instrument described here provides a measure of ion current entering an orifice where only those ions having energies above some threshold are counted. In this way it differs from a class of instruments, curved-plate electrostatic analyzers, which respond to particles within a band of energies. Though the theory pertains to either electrons or ions, the implementation described here is for ions.

The traditional Faraday cup has generally consisted of an orifice and a collector plate separated by several biased grids. Current reaching the collector is detected by an electrometer as a programmed sequence of voltages is applied to the grids. Problems in the use of these instruments have been numerous and are detailed in Appendix I. Of particular interest for ion collection are sensitivity to photons, grid-wire spacing effects, Mach effects, acceptance cone, sheaths, and response time.

Generally Mach effects and sheaths will be present and should be accounted for in the theory of the device; a way of doing this has been presented by Whipple, Warnock, and Winkler (Ref. 1). Included in their calculations is the effect of a wide-angle acceptance cone which is typical for a Faraday cup.

This report considers a special case of the aforementioned work, that where ions are received only through a narrow acceptance angle as measured from the normal to the face of the instrument. The restriction in angle has several beneficial effects, not only simplifying the theoretical formulation but also allowing a simple instrument design to be implemented. If ions can approach a biased grid from various angles, the criteria for passing through the grid depends on angle as well as ion energy. Restriction to near-normal incidence thus removes one complicating factor in the theory. Another feature of the general theory, the dependence of instrument response on sheath size, is also made unnecessary by the small-angle restriction. These simplifications allow replacing the numerical quadratures of the general theory with closed-form solutions. The proposed design allows for eliminating grids, for separating photons and ions to render the instrument insensitive to photons, and for achieving high sensitivity with a particle counter which is used in place of an electrometer.

In this report the general formulation of the problem is modified for the small-angle case, the integrals are evaluated, possible applications are discussed, and laboratory tests of prototype instruments are presented.

THEORETICAL FORMULATION

The equations and notation of Whipple, Warnock, and Winkler (Ref. 1) are taken as the starting point for this development. Their constraints on the range of integration are included and then further restrictions are imposed by the specifications on angle of incidence. With these restrictions, upper and lower bounds on the integrals can be established. When the limits are sufficiently close to each other, a simplified integral can be used for practical computations.

Summary of Work by Whipple, Warnock, and Winkler

The current to an ion measuring instrument is

$$I = AJ_oJ \tag{1}$$

where A is the area of the orifice, J_o is the random current density given by

$$J_o = ne(kT/2\pi m)^{1/2} \tag{2}$$

and where

$$J = \exp(-V_s-M^2) \iint\limits_{\substack{\text{Allowed}\\ X,Z}} F\, dx\, dz$$

$$\cdot \exp(-Z-X+BE^{1/2} \cos \alpha_\infty)\ I_o(DE^{1/2} \sin \alpha_\infty) \tag{3}$$

The function F is assumed to be unity in the referenced work and the notations, $B=2M \cos\gamma$ and $D=2M\sin\gamma$, are newly introduced here. Other symbols are as previously defined and are summarized in the symbol table. Symbols are defined with reference to the system shown in Fig. 1. It is especially important to note the condition of energy conservation

$$E = X + Z + V_s \tag{4}$$

where all quantities are energies normalized by the factor kT, X and Z are

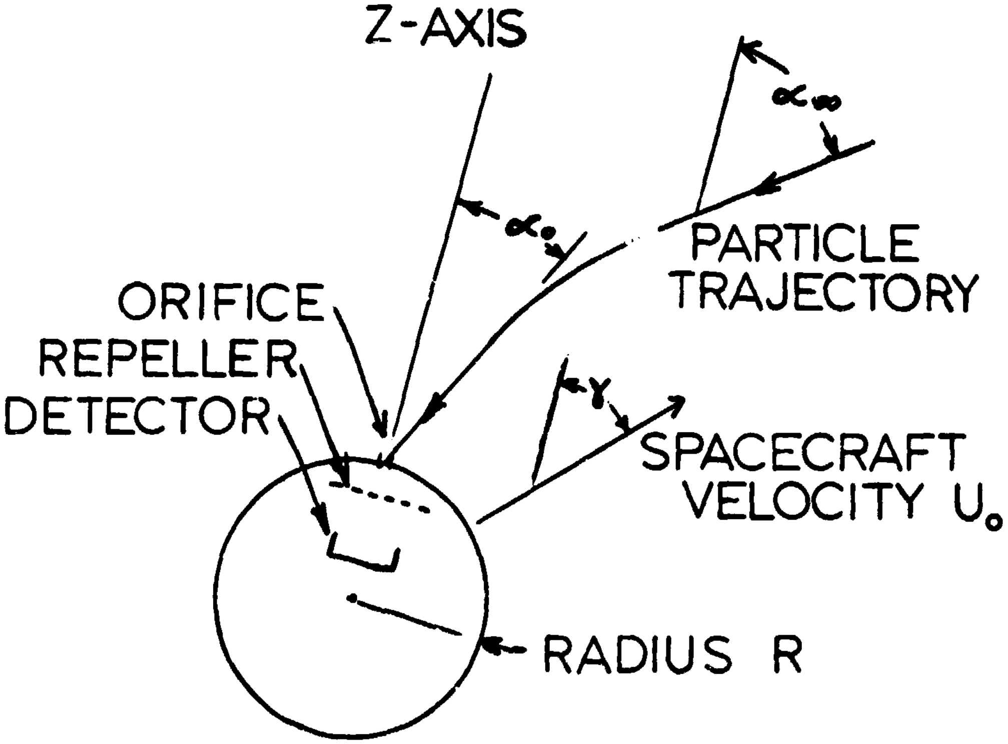

Fig. 1. A spacecraft model which shows a coordinate reference system used for defining symbols.

tangential and normal kinetic energies of a particle at the orifice of the instrument, and V_s is the normalized energy derived from spacecraft potential. Mach number is M and sheath size is imbedded in α_∞ as well as the integration limits.

A spherical conductive spacecraft of radius R is assumed to have a sheath defined in terms of the parameter $L = \gamma/R$ where γ is Debye length and L varies from 0 to ∞. This parameter relates the angles of incidence measured at the orifice α_o and measured outside the sheath α_∞. Note that $\tan^2 \alpha_o = X/Z$. Specifically it may be shown that, for $L = 0$,

$$\begin{aligned} \sin \alpha_\infty &= \sqrt{\frac{E-V_s}{E}} \sin \alpha_o \\ E \sin^2 \alpha_\infty &= X \\ E \cos^2 \alpha_\infty &= Z+V_s \end{aligned} \tag{5}$$

and, for $L = \infty$,

$$\begin{aligned} \alpha_\infty &\approx \sqrt{\frac{E-V_s}{E}} \sin \alpha_o, \text{ large E} \\ \alpha_\infty &\approx 2\alpha_o \qquad\qquad , \text{ small E} \end{aligned} \tag{6}$$

When $V_s < 0$ (attractive to ions) and $\alpha_o \approx \sin \alpha_o$, the ratio of α_∞/α_o is as shown in Fig. 2 . Thus for some point X,Z one may infer that

$$\begin{aligned} \sin \alpha_\infty &\leq \sin \alpha_\infty\big|_{L=0} \\ \cos \alpha_\infty &\geq \cos \alpha_\infty\big|_{L=0} \end{aligned} \tag{7}$$

The allowed range of integration is subject to constraints. First one must have $E \geq 0$ or $X+Z \geq -V_s$. This boundary is identified by the parameter $L=\infty$ in Fig. 3. In addition the requirement that trajectories not start elsewhere on the spacecraft places a further constraint shown by the various L parameters. When V_s is positive one simply requires that $X > 0$ and $Z > 0$, and in any case the repeller bias condition is that $Z > V_g$, where V_g is the normalized repeller voltage.

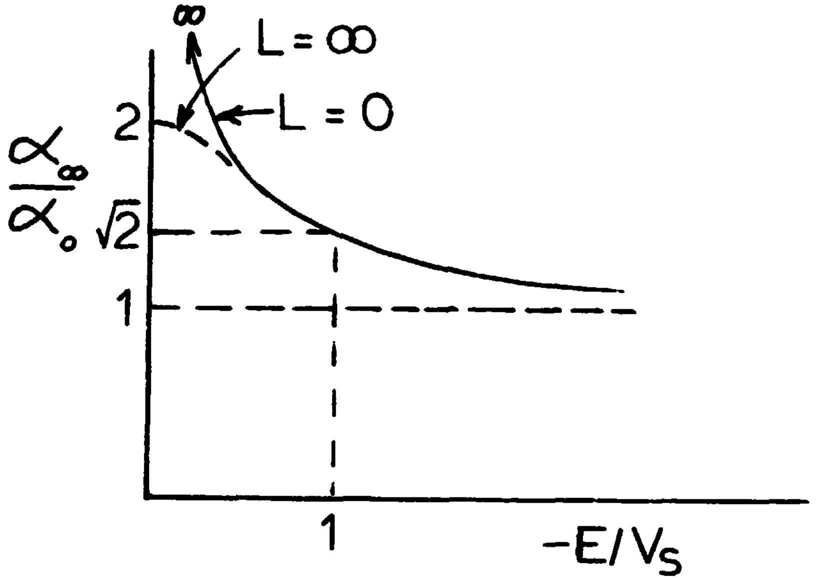

Fig. 2. The ratio of α_∞/α_o for various L values and small α's.

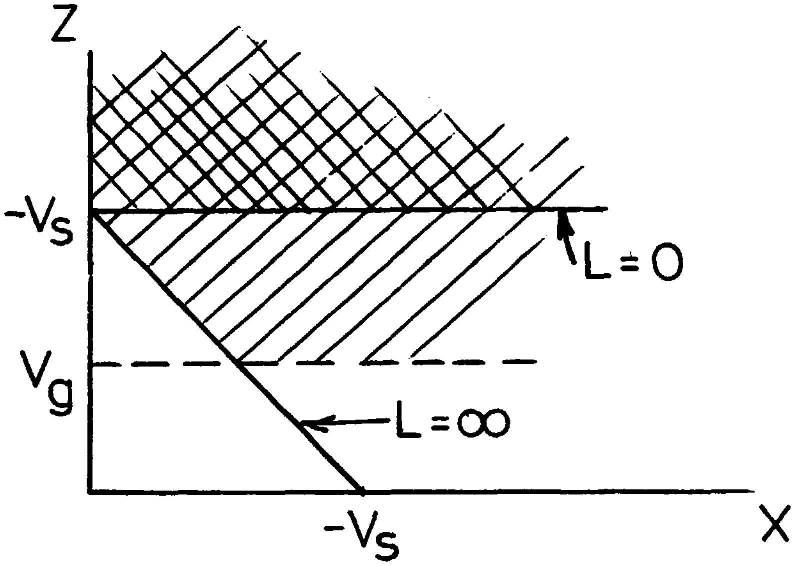

Fig. 3. Allowed ranges of integration for Eq. 3 for various L values.

Function Bounds

When L=0 the Modified Bessel function simplifies as follows:

$$I_o(D\sqrt{E}\ \sin \alpha_\infty)\Big|_{L=0} = I_o(D\sqrt{X}) \tag{8}$$

Consequently for any L, by use of Eq. 7,

$$1 \leq I_o\ (D\sqrt{E}\ \sin \alpha_\infty) \leq I_o(D\sqrt{X}) \tag{9}$$

It is convenient to use a series representation

$$I_o(D\sqrt{X}) = 1 + \frac{D^2X}{4} + \frac{D^4X^2}{64} + \frac{D^6X^3}{2304} + \cdots. \tag{10}$$

In similar fashion one may write

$$B\ E^{1/2}\ \cos \alpha_\infty\Big|_{L=0} = B\sqrt{V_s+Z}\ . \tag{11}$$

Also by definitions

$$B\ E^{1/2} \leq B\sqrt{V_s+WZ} \tag{12}$$

where $W \equiv 1+U$ and $U \equiv (X/Z)_{max}$.

Thus for any L, one may write

$$B\sqrt{V_s+Z} \leq B\ E^{1/2}\ \cos \alpha_\infty \leq B\sqrt{V_s+WZ} \tag{13}$$

Small-angle Restriction

When the instrument is designed so that ions can enter only at some small angle $\alpha \leq \alpha_o$, then the range of integration is modified as shown in Fig. 4. This is the same as Fig. 3 with the additional restriction that $X \leq UZ$. A conceivable design to limit the angle is to place two circular orifices in a row such that only particles passing through both would be detected. Fig. 5 shows this arrangement where the smaller of the two orifices fixes area $A = \pi D_2^2/4$ and the larger of the two fixes U:

$$U = \left(\frac{D_1}{2S}\right)^2. \tag{14}$$

This result is applicable if $D_1 >> D_2$ and for this case the parameter F in Eq. 3 is unity.

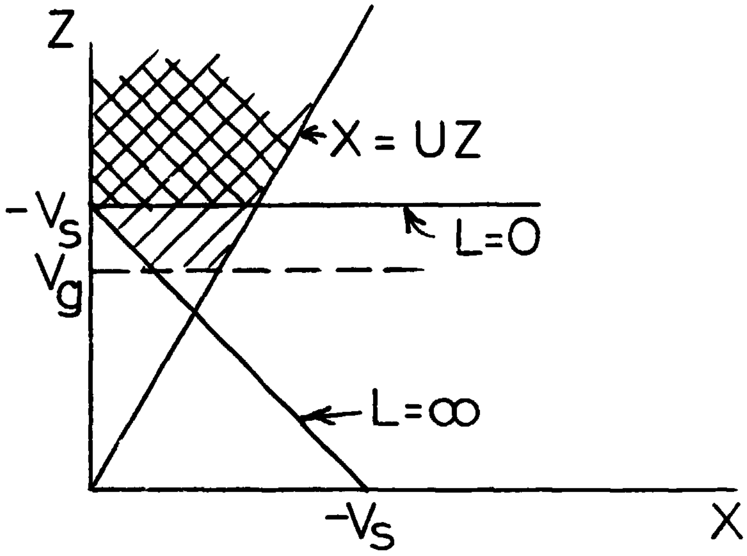

Fig. 4. Allowed ranges of integration for Eq. 3 when a constraint is placed on the angle of incidence.

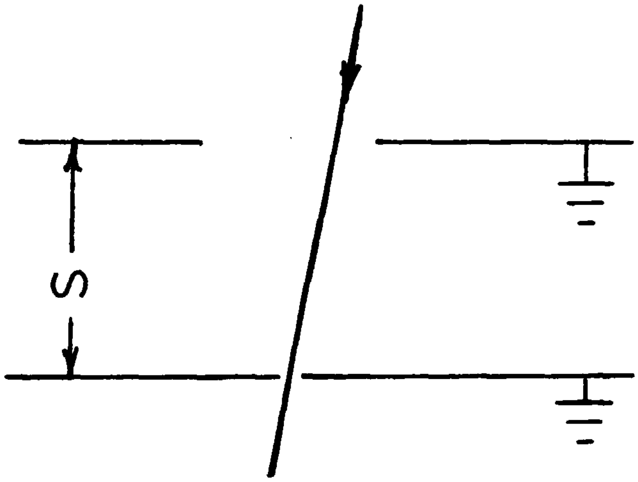

Fig. 5. Trajectory of particle passing through upper and lower circular orifices having diameters D_1 and D_2 respectively.

A more practical system uses two orifices of equal diameter as shown in Fig. 6. Here $A = \pi D^2/4$ as before but U differs:

$$U = (\frac{D}{S})^2 \tag{15}$$

Most importantly the function F is unity only for $\alpha=0$ and otherwise it is less than unity.

For nonnormal incidence, the effective area is less than that of a single hole. Figure 7 shows the geometry on which is based a calculation of the reduction factor F.

The parameters β and C are found from

$$C = S(\tan\alpha_o)/2 \tag{16}$$

and

$$\beta = \arccos\ (2C/D). \tag{17}$$

Then the area A' can be expressed as

$$A' = \beta\ D^2/4 - C^2\ \tan\beta \tag{18}$$

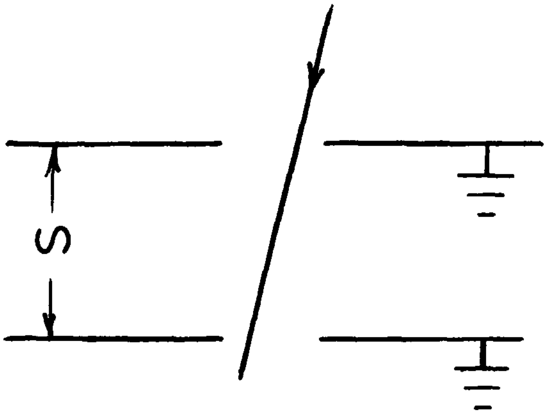

Fig. 6. Trajectory of particle passing through equal circular orifices having diameter D.

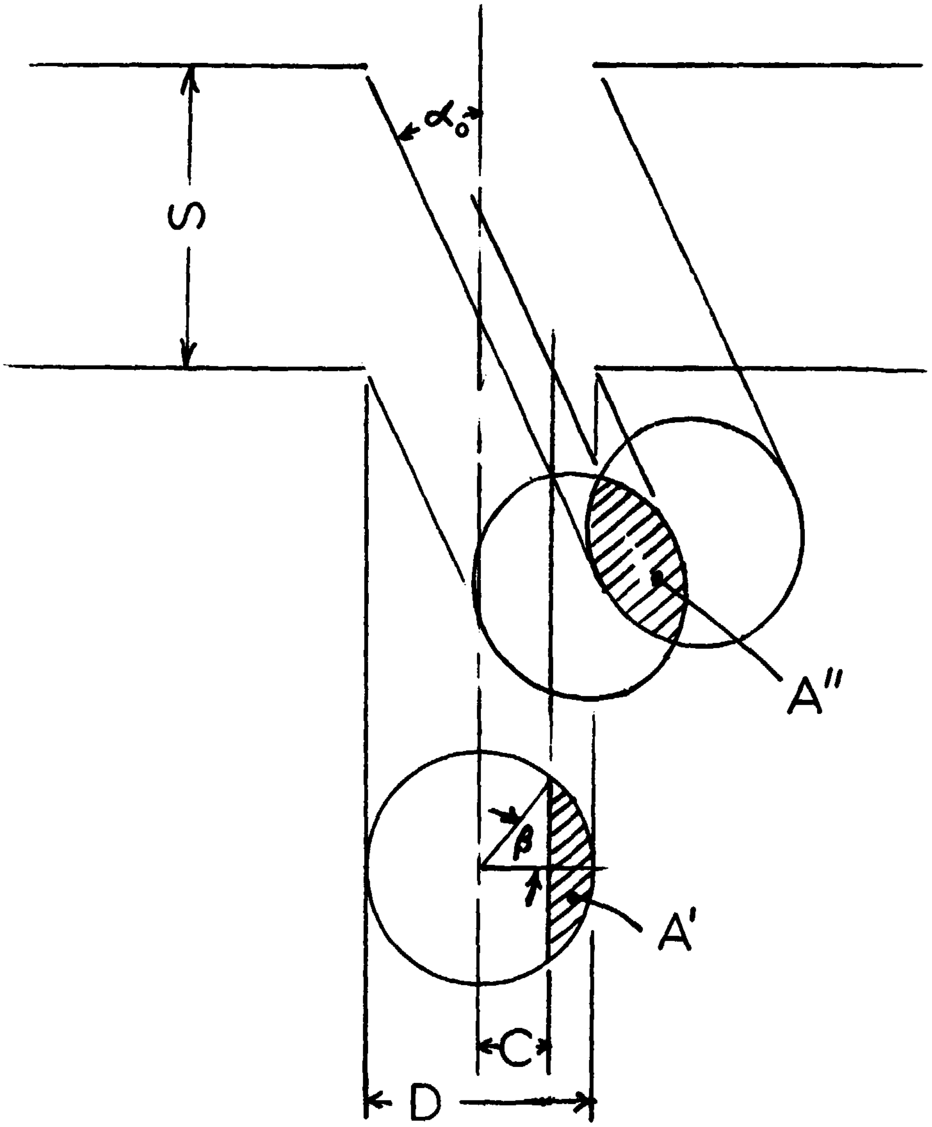

Fig. 7. Computation of the effective area A" which is seen by particles having an angle of incidence α_o.

The foreshortened area A" is given by

$$A'' = 2A' \cos \alpha_o \tag{19}$$

which is the effective area seen by particles at the angle α_o. The function F is found by comparing A" with A cos α_o and it is found to be

$$F = \frac{\beta D^2/2 - 2C\ ^2 \tan\beta}{\pi D^2/4} \tag{20}$$

or

$$F = \frac{1}{\pi}(2\beta - \sin(2\beta)).$$

Equations 15-17 combine to show that

$$\beta = \arccos T = \pi/2 - \arcsin T \tag{21}$$

where $T \equiv \sqrt{\frac{X}{UZ}}$. Series expansions in T yield

$$\beta = {}^{\pi}/2 - (T + \frac{1}{2}\frac{T^3}{3} + \frac{1}{2}\frac{3}{4}\frac{T^5}{5} + \cdots) \tag{22}$$

and

$$\sin 2\beta = 2T\sqrt{1-T^2} = 2T(1 - \frac{1}{2}T^2 - \frac{1}{8}T^4 - \frac{1}{16}T^6 \cdots). \tag{23}$$

Consequently the final expression for F is series form is

$$\begin{aligned} F = 1 - (\tfrac{4}{\pi})\ T + (\tfrac{2}{3\pi})\ T^3 + (\tfrac{1}{10\pi})\ T^5 + (\tfrac{1}{28\pi})\ T^7 \\ + (\tfrac{1}{57.6\pi})\ T^9 + \cdots,\ 0 \leq T \leq 1 \end{aligned} \tag{24}$$

where the coefficients $-\frac{4}{\pi}$, $\frac{2}{3\pi}$, $\cdots$ are conveniently designated F_1, F_3, $\cdots$. Though this form seems unwieldly compared with Eq. 20 it is well suited when the integral of Eq. 3 is evaluated. The function F is illustrated in Fig. 8.

Basic Integral

The inequalities of Eqs. 9, 13 may be used to set upper and lower bounds on the integral of Eq. 3, which is rewritten here in a form adaptable to identifying the bounds:

$$\begin{aligned} J = \exp(-V_s - M^2) \int_V^{\infty} dZ \exp(-Z + B\sqrt{ZW+V_s}) \\ \cdot \int_0^{UZ} dX\ F\left(\sqrt{\frac{X}{UZ}}\right) \exp(-X)\ I_o(D\sqrt{X}) \end{aligned} \tag{25}$$

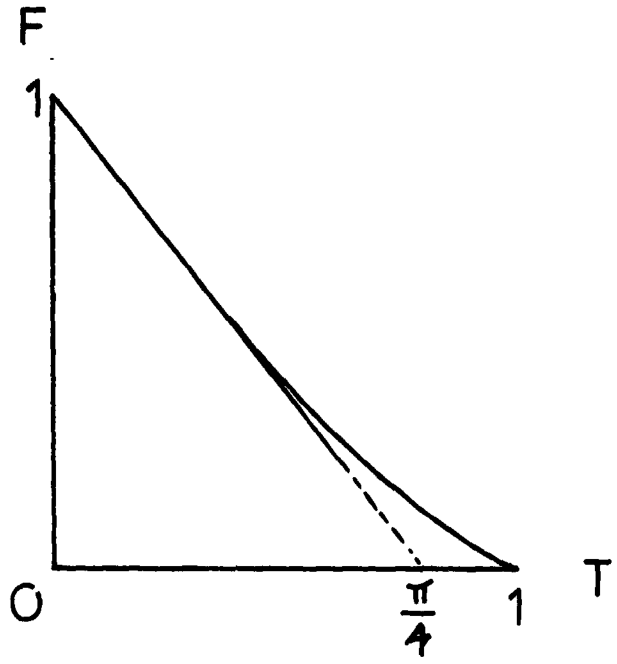

Fig. 8. The function F(T) which represents the decrease in aperture area associated with nonnormal incidence.

The lower limit V is to be the largest of $-V_s$, 0, and V_g where V_s is the normalized potential of the spacecraft relative to the space plasma and V_g is the normalized grid potential relative to the spacecraft. Note that in practice a grid is not used but rather a biased drift tube.

For special case where $-V_s > V_g$, $-V_s > 0$, and $L \neq 0$, the range specified for the integral, Eq. 25, will be incorrect as Fig. 9 illustrates. The contribution ΔJ from the double-hatched region will be bounded as follows:

$$0 \le \Delta J \le \exp(-V_s - M^2) \int\int dX\, dZ. \qquad (27)$$
$$\cdot \exp(V_s + |B|\sqrt{-UV_s})\; I_0(D\sqrt{-UV_s})\; (UV_s)^2/2$$

This correction, which depends on the second power of U, is usually found to be negligible. Consequently one may choose the limits from V to ∞ as if $L=0$.

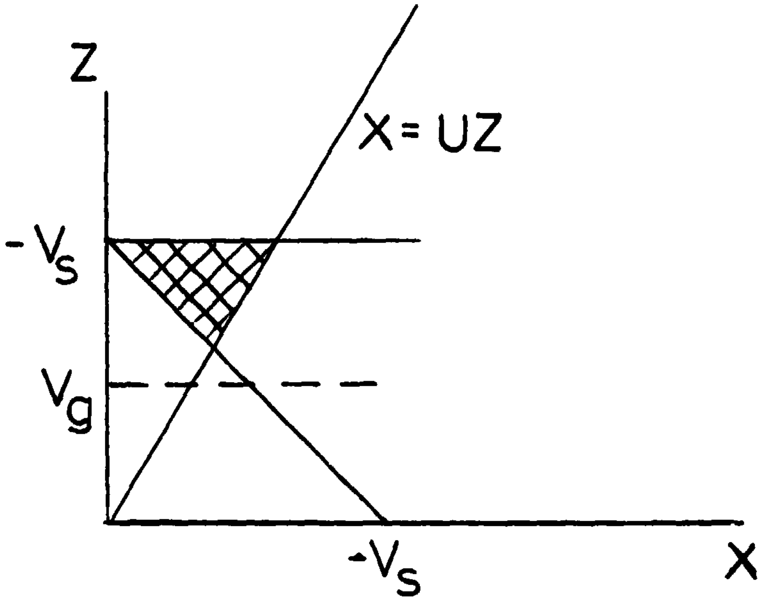

Fig. 9. The region excluded from the approximate integral formulation given by Eq. 25.

Aside from the possible contribution of ΔJ one may then specify bounds on Eq. 25 as shown in Table 1. The second case shown is more simple to evaluate than the others and it can be used to calculate the instrument response when the bounds are acceptably close together. The explanation for the existence of the bounds comes from the inequalities previously noted. Though W has been defined as 1+U so as to set the upper bound in Eq. 13, one may obtain the lower bound from W=1. In like manner the upper bound in Eq. 9 corresponds to use of D as it is defined. Setting D=0 produces the lower bound.

In this section the integral of Eq. 3 has been transformed into Eq. 25 which is a form appropriate for analzying response of an instrument having a restricted angle of incidence. Table 1 summarizes several special cases of interest and Eq. 27 provides a correction to the upper bound. The function F shown in Eq. 24 is appropriate for the case of two equal aperatures, and it is used in the next section which describes the evaluation of the integral.

TABLE 1. Choices of Parameters which Yield Upper and Lower Bounds.

B	D	W	VALUE OF INTEGRAL
> 0	Itself	1 + U	J^{*}_{max}
	0	1	J_{min}
< 0	Itself	1	J^{*}_{max}
	0	1 + U	J_{min}

*Increase by ΔJ from Eq. 27 to obtain upper bound.

EVALUATION OF THE INTEGRAL

The integral Eq. 25 contains two variables of integration, X and Z. Integration over X is done first and the result is expressed as a power series in U, which is the maximum value of X/Z. When U is small, as is the case for the prototype systems described in a later section, then the first term of the series often suffices. The integral over Z is done analytically without further approximations being made.

X-Integration

A portion of Eq. 25 may be identified as the X-integral:

$$J_X = \int_0^{UZ} dX \; F\left(\sqrt{\frac{X}{UZ}}\right) \exp(-X) \; I_o(D\sqrt{X}) \tag{28}$$

If the series expansions (see Eq. 10, 24) for I_o, F, and exp(-X) are multiplied together and (28) is integrated term by term, then the results may be collected by powers of U:

$$\begin{aligned} J_X = {} & UZ \; [1 + \tfrac{2}{3} F_1 + \tfrac{2}{5} F_3 + \tfrac{2}{7} F_5 \cdots] \\ & + (UZ)^2 [\tfrac{D^2}{4} - 1] \; [\tfrac{1}{2} + \tfrac{2}{5} F_1 + \tfrac{2}{7} F_3 + \tfrac{2}{9} F_5 \cdots] \\ & + (UZ)^3 [\tfrac{D^4}{64} - \tfrac{D^2}{4} + \tfrac{1}{2}] \; [\tfrac{1}{3} + \tfrac{2}{7} F_1 + \tfrac{2}{9} F_3 + \tfrac{2}{11} F_5 \cdots] \end{aligned} \tag{29}$$

Note that the F_i's are the coefficients of Eq. 24 for the case of two equal apertures and the F_i's are all zero if one aperture is large compared with the other. The integral J_X may be written simply as

$$J_X = \sum_{i=1}^{\infty} (UZ)^i A_i \tag{30}$$

where the A_i's are given in Table 2. Values up to F_9 have been retained in evaluating the A_i's because the F-series is slowly convergent.

Z-Integration

When J_X from Eq. 30 is substituted into Eq. 25, the expression for J becomes

$$J = \exp(-V_s - M^2) \int_V^{\infty} dZ \; \exp(-Z + B\sqrt{V_s + WZ}) \sum_{i=1}^{\infty} (UZ)^i A_i . \tag{31}$$

TABLE 2. Values of A_i

One aperture much larger than other	A_1	1
	A_2	$(\frac{D^2}{4} - 1)\ (\frac{1}{2})$
	A_3	$(\frac{D^4}{64} - \frac{D^2}{4} + \frac{1}{2})(\frac{1}{3})$
Equal apertures	A_1	0.249
	A_2	$(\frac{D^2}{4} - 1)(0.061)$
	A_3	$(\frac{D^4}{64} - \frac{D^2}{4} + \frac{1}{2})(0.025)$

A change of variable is instituted through the definition:

$$H^2 = \frac{B^2W}{4} + \frac{V_s}{W} + Z - B\sqrt{V_s+WZ} \tag{32}$$

This may be solved for Z explicitly:

$$Z = H^2 + \frac{B^2W}{4} - \frac{V_s}{W} + B\sqrt{WH^2} \tag{33}$$

From this the differential dZ is found to be

$$dZ = (2H + B\sqrt{W})\ dH. \tag{34}$$

In these equations B may be either negative or positive depending on whether the Mach angle γ exceeds 90° or not. In terms of the new variable H the expression for J is

$$J = \exp\left(-V_s + \frac{V_s}{W} - M^2 + \frac{B^2W}{4}\right) \int_G^{\infty} dH \exp(-H^2)(2H+B\sqrt{W}) \cdot \sum_{i=1}^{\infty} A_i U^i \left(H^2 + \frac{B^2W}{4} - \frac{V_s}{W} + HB\sqrt{W}\right)^i \tag{35}$$

where the limit G is

$$G = \left(\frac{B^2W}{4} + \frac{V_s}{W} + V - B\sqrt{V_s+WV}\right)^{1/2}. \tag{36}$$

This limit of integration may be negative for certain conditions as shown in Fig. 10. Always the limit V will be subject to the conditions

$$V \geq 0\ ,\ V \geq -V_s \tag{37}$$

The expression for J contains integrals of the form,

$$I_i = \int_G^{\infty} H^i \exp(-H^2)\ dH \tag{38}$$

several of which are shown in Table 3. The integrals are used as needed in developing the expressions for J which follow.

Equation 35 for J may be expressed in terms of J_i's as follows:

$$J = \exp\left(-V_s + \frac{V_s}{W} - M^2 + \frac{B^2W}{4}\right) \sum_{i=1}^{\infty} A_i U^i\ J_i \tag{39}$$

Typically only i=1 will be of interest yet expressions for both J_1 and J_2

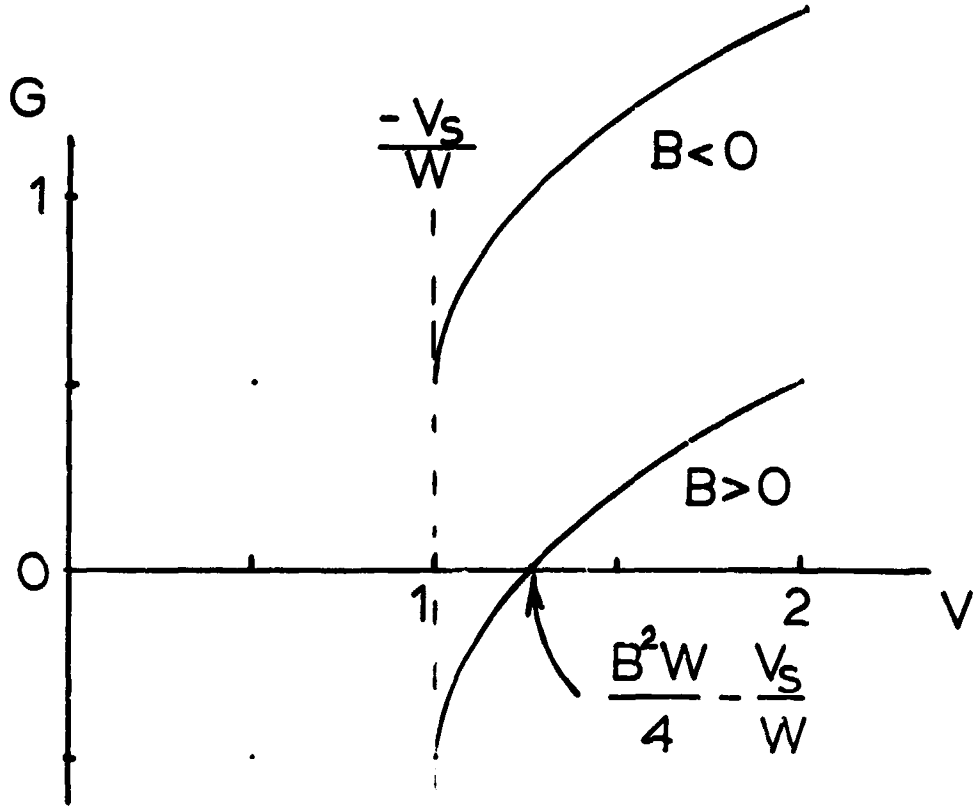

Fig. 10. Evaluation of the lower limit G illustrated for the case W=1, V_s=−1, B=±1.

are given below. The general form for J_i is

$$J_i = \int_G^\infty dH \exp(-H^2)(2H+B\sqrt{W})(H^2+HB\sqrt{W} + \frac{B^2W}{4} - \frac{V_s}{W})^i \tag{40}$$

or in simpler notation

$$J_i = \int_G^\infty 2dH \exp(-H^2)(H+a)(H^2+2aH+b)^i \tag{41}$$

where $a = B\sqrt{W}/2$ and $b = a^2 - V_s/W$.

Consequently one finds that

$$J_1 = (2G^2 + 6aG + 2 + 4a^2 + 2b)\, I_1 + (3a + 2ab)\, I_o \tag{42}$$

$$\begin{aligned} J_2 = {} & [2G^4 + 10\, aG^3 + (4 + 16a^2 + 4b)G^2 \\ & + (30a/2 + 8a^3 + 12ab)\, G \\ & + (4 + 16a^2 + 4b + 2b^2 + 8a^2b)]\, I_1 \\ & + [15a/2 + 4a^3 + 2ab^2 + 6ab]\, I_o \end{aligned} \tag{43}$$

TABLE 3. Integrals I_i

I_o	$\sqrt{\pi}\ \mathrm{erfc}(G)/2$
I_1	$\exp(-G^2)/2$
I_2	$GI_1 + I_o/2$
I_3	$(G^2 + 1)\ I_1$
I_4	$(G^3 + 3G/2)\ I_1 + 3I_o/4$
I_5	$(G^4 + 2G^2 + 2)\ I_1$
I_n	$G^{n-1}\ I_1 + (n-1)\ I_{n-2}/2$

The integration is thus complete in a general form which appears somewhat cumbersome but which is adapted in rather simple form to numerous cases described next. The most general solution is formed by combining Eq. 42, 43 for J_1 and J_2 with the expression for J given as Eq. 39. The A_i coeffients come from Table 2, the limit G from Eq. 36, and the integrals I_1, I_o from Table 3.

SPECIAL CASES AND APPLICATIONS

The general formulation presented in the previous section may be interpreted in numerous ways. Several special cases are described here: spherical probe, unbiased stationary sphere, biased spheres with 0° and 90° Mach angles, and the general equations divested of the parameters used tc estimate bounds. Then typical parameters are summarized for various measurements which have been reported in the literature.

Sperical Probe

The equations for a spherical probe may be derived for the special case that $V_g = 0$, i.e., there is no discrimination in terms of the energies of particles entering the orifice of the instrument. Also it is assumed that the probe is stationary in the plasma, M=B=D=0. Furthermore F is assumed to be unity. If the probe is positively biased ($V_s > 0$) then $V = 0$, and for this repulsive mode of operation:

$$G^2 = V_s/W, \; A_1 = 1, \; A_2 = -\frac{1}{2} \tag{44}$$

Also:

$$J_1 = 2I_1 \; , \; J_2 = 4I_1 \tag{45}$$

Consequently, with reference to Eqs. 1, 39,

$$I = AJ_o \exp(-V_s) \; (U - U^2 \cdots) \tag{46}$$

This is the usual expression for current collected by a repulsive probe except for the factor $(U-U^2 \cdots)$ which accounts for the restricted angle of incidence.

For the case where the probe attracts ($V_s < 0$), one uses $V = -V_s$ and $G^2 = V_s/W - V_s$. The integral J_1 then becomes

$$J_1 = \exp(-G^2)(1-V_s) \tag{47}$$

and if J_2 is ignored then I becomes

$$I = AJ_o \; (1-V_s)U. \tag{48}$$

This, aside from the factor U, is the equation for an attracting spherical probe.

Unbiased Stationary Sphere

Another relatively simple case has $V_s = 0$ and $V_g > 0$ where again, $M=B=D=0$ and $F=1$. The response for $V_g < 0$ is the same as for $V_g = 0$. For this case:

$$A_1=1,\ A_2 = -\frac{1}{2}$$

$$J_1 = (1+V_g)\ \exp(-V_g) \tag{49}$$

$$J_2 = (V_g{}^2+2V_g+2)\exp(-V_g)$$

The current is found to be

$$I = AJ_o\ \exp(-V_g)[U(1+V_g) - U^2(V_g{}^2/2 + V_g + 1)\cdots] \tag{50}$$

Biased Sphere with Zero Mach Angle

For this case it is assumed that $V_s = -1$ making the sphere attractive, that $M= 1/2$, and that $\gamma=0$. Consequently $B=1$ and $D=0$. It is also assumed for illustration that $U = 0.01$ and that $F=1$. The lower bound for the integral corresponds to $W=1$ such that

$$A_1=1,\ A_2= -1/2,\ a= 1/2,\ b= 5/4 \tag{51}$$

$$G^2= -3/4 + V_g - \sqrt{-1+V_g}$$

Using these values one may show that

$$J_1 = \exp(-G^2)\ (G^2 + 3G/2 + 11/4) + 11\sqrt{\pi}\ \text{erfc}(G)/8. \tag{52}$$

A similar calculation may be done for $W=1.01$ which corresponds to the upper bound. Results for both values of W are shown in Fig. 11 which includes only the J_1 term. Inclusion of the J_2 term at the point $V_g = 1$ yields (with $G= -1/2$)

$$I = AJ_o(5.458\ U - 9.047\ U^2 \cdots)$$

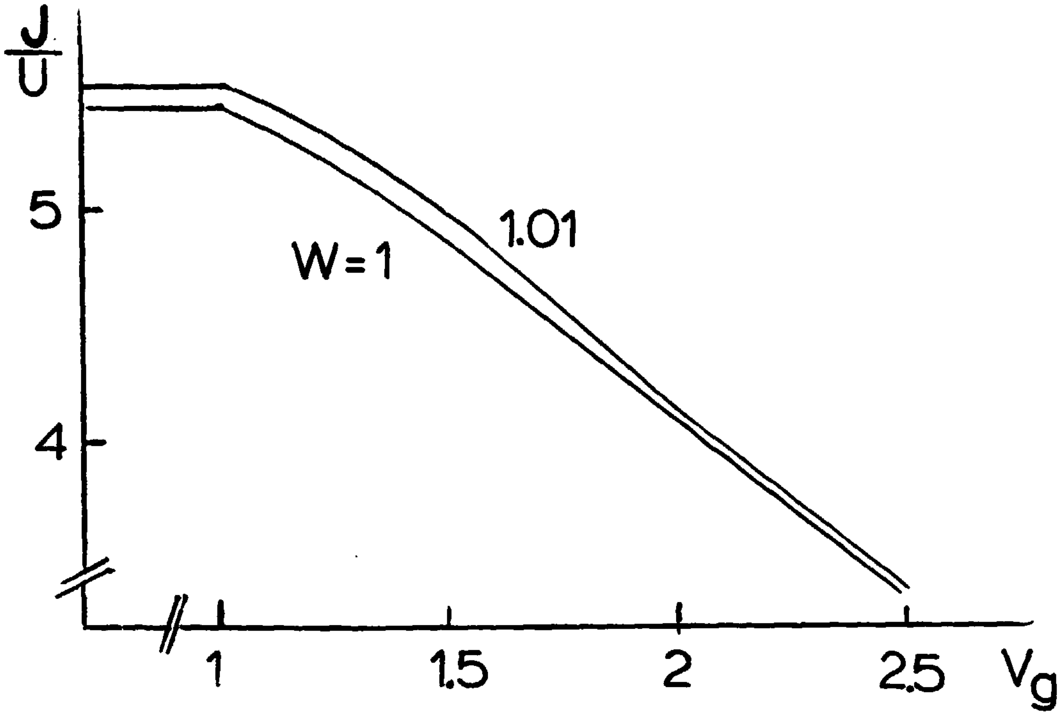

Fig. 11. Bounds on J/U for U=0.01, B=1, D=0, and F=1. Only J_1 is included in the calculation.

from which it is seen that the J_2 term containing U^2 represents a correction of less than 2 percent. The correction ΔJ from Eq. 27 applies only if $V_g < 1$ and it has an upper bound of

$$\Delta J/U \leq 4.3\text{x}10^{-3} \tag{53}$$

which is about 0.1 percent. If one is willing to ignore the various uncertainties amounting to at most 3%, then he can use the case for W=1 without J_2 to write an expression for current as a function of grid bias:

$$I = AJ_o \; U \; J_1 \tag{54}$$

Here J_1 and G are as defined by Eqs. 51 and 52.

The numbers and results shown in this case are considered to be a typical application though of course the equations cease to be useful if, for some combination of parameters, the bounds are not sufficiently tight. The general equations as formulated in this report allow one to estimate the possible error in the use of a simpler equation such as (54).

Biased Sphere with 90° Mach Angle

Parameters are the same here as for the previous case except that $B=0$ and $D=1$. Consequently $W=1$, $G=\sqrt{V_g-1}$, $A_1=1$, $a=0$, and $b=1$. The parameter A_2 depends on D which will be 1 for the upper bound and 0 for the lower bound. Thus A_2 may be $-3/8$ or $-1/2$, respectively. Consequently the instrument response is

$$I = AJ_o \exp(-G^2-1/4)\ [U(G^2+2) - U^2(G^4/2 + 2G^2 + 5/2)\cdots] \tag{55}$$

If $V_g = -V_s$ which is the condition for maximum I, then $G=0$ and

$$I = AJ_o \exp(-1/4)\ [2U - 5U^2/2\ \cdots] \tag{56}$$

The above expressions yield the lower bound with $D=0$, the upper bound is found by reducing the U^2 term by the factor 3/4. When the U^2 term is ignored, the result becomes

$$I = AJ_o \exp(3/4 - V_g)\ U\ (V_g + 1) \tag{57}$$

Note that for the special case $B=0$, the value of W is immaterial. The same result is obtained for either $W=1$ or $W=1+U$.

Simplified Equations

When one has justified that the bounds are sufficiently tight by considering the various cases of Table 1, then it is expedient to work with the response in simplified form. To do this one assumes $W=1$ and $J_2=J_3\cdots=0$. Consequently one has

$$G^2 = B^2/4 + V_s + V - B\sqrt{V_s+V} \tag{58}$$

and the constant A_1 may have either of two values, 1 or 0.249, depending on the choices of aperture diameters. Then

$$I = AJ_o \exp(-M^2+B^2/4)\ A_1\ U\ J_1 \tag{59}$$

where

$$J_1 = \exp(-G^2)(G^2+3BG/2 + 1 - V_s + 3B^2/4) \tag{60}$$
$$+ \sqrt{\pi}\ \mathrm{erfc}(G)\ (3B/4 + B^3/8 - BV_s/2)$$

In these expressions the value of B may range from +2M to -2M as the Mach angle changes. As previously given, V is the largest of 0, $-V_s$, and V_g. The value of G will be negative if $V < B^2/4 - V_s$ and $B > 0$.

Possible Uses

Numerous measurements have been made where the proposed instrument and its theoretical interpretation would have been applicable. Some of these are summarized here.

Whipple, Warnock, and Winkler [Ref. 1] were able to adjust the parameters of ion temperature, spacecraft potential, and sheath size until their theoretical predictions matched the data of OGO 3. Ion density was also found from the normalization factor J_o. The equations developed here can be used similarly except that sheath size is not needed nor can it be inferred from the data.

Whipple, Warnock, and Winkler [Ref. 1] refer to OGO 3 measurements where ion temperature varied from 4000 to 20,000 K and the corresponding factor kT/e from 0.34 to 1.7 ev. For satellite potentials to -5V, the normalized potential $-V_s$ could be as large as 16 in the plasma sphere but less than 1 beyond the plasmapause. Mach number M was typically less than unity and substantially less beyond the plasmapause for hydrogen. The spread on the bounds of the integral increases with B and with $-V_s$. Typical percentage uncertainties in J are given in Table 4. Obviously one would try to keep spacecraft potential from being much larger than the ion temperature (in eV) if small error bars are sought.

Harris [Ref. 2] advocates the measurement of cold ion density in the plasma trough as an important diagnostic tool and, in a related paper, Chappell [Ref. 3] describes detached regions of the plasma sphere which have densities several hundred times the usual trough density of about

10^6 ion/m^3. An ion sensor as described in this report could provide information about the cold (ie, thermal) ions in the plasma sphere and beyond.

Sensitivity analysis can be based upon the simplified form given by Eqs. 59, 60. Assume that $A = 0.785 \times 10^{-6} m^2$, $A_1 = 0.249$, and $U = 0.0062$, where these values correspond to a prototype which has been laboratory tested. Random current density at 4000°K is, for hydrogen, $J_o = 3.68 \times 10^{-16} n$ (A) or, with a particle counter, 2300n (Hz) where n is in m^{-3}. For an M of 0.5, a B of 1, and $V_g = - V_s = 10$,

$$I = 0.0380 \, A \, J_o = 69 \times 10^{-6} n \text{ (Hz)}.$$

Because the background counting rate is typically 0.2 Hz, then a density of $1.4 \times 10^4 m^{-3}$ will be detectable at a rate of about 1 Hz. At the other extreme, counting rates as high as 10^5 Hz are possible without pulse overlap, this corresponding to a density greater than $10^9 m^{-3}$. The sensitivity of an instrument can be set through the choosing of the aperture area and the separation between apertures; a pair of instruments can cover complementary ranges.

TABLE 4

Typical Percentage Uncertainties in J Values

$-V_g$	V_g	M	B	U	Percent Difference $J_{max}-J_{min}$	Percent Error if J_2 is Neglected
10	10	1	2	0.01	10.	+3.1
10	10	1	2	0.0062	6.2	1.9
10	10	0.5	1	0.0062	3.7	1.8
10	10	0.5	0	0.0062	0.0	1.5
1	1	0.5	1	0.0062	0.7	0.5
1	4	0.5	1	0.0062	0.8	0.8

DESIGN AND TESTING OF A PROTOTYPE

The preceding theoretical development provides a basis for the design of an instrument to measure thermal ion density and temperature. The key requirements are that the instrument accept ions from a small viewing cone, that it provide an internal retarding potential for rejecting ions having energies below an adjustable threshold, and that the entrance orifice be biased more negatively than the local plasma potential unless some other means exists for measuring spacecraft potential. Then from the data and with a calibrating measurement of sensitivity, one may calculate the ion density, the ion temperature, and the spacecraft potential.

The retarding potential in the instrument should be stepped through a sequence of values ranging from zero to, say, 5 V more than the sum of any negative bias on the instrument itself plus the maximum negative excursion in spacecraft potential which is anticipated. However, for resolution one wants perhaps several steps per volt. Thus a compromise arises involving resolution, range of spacecraft potential, and telemetry rate. The usefulness of the instrument can be extended to times when negative charging would otherwise disrupt operation by operating an electron emitter in such a way as to stabilize spacecraft potential.

Instrument Design

A prototype instrument has been constructed as shown in Fig. 12 to demonstrate the feasibility of detecting ions subject to the criteria of small viewing cone and energy selection. The instrument was enclosed in a grounded stainless steel can, which was supported on pivots. The can could be rotated about an axis passing through the entrance orifice and lying in the plane of the orifice.

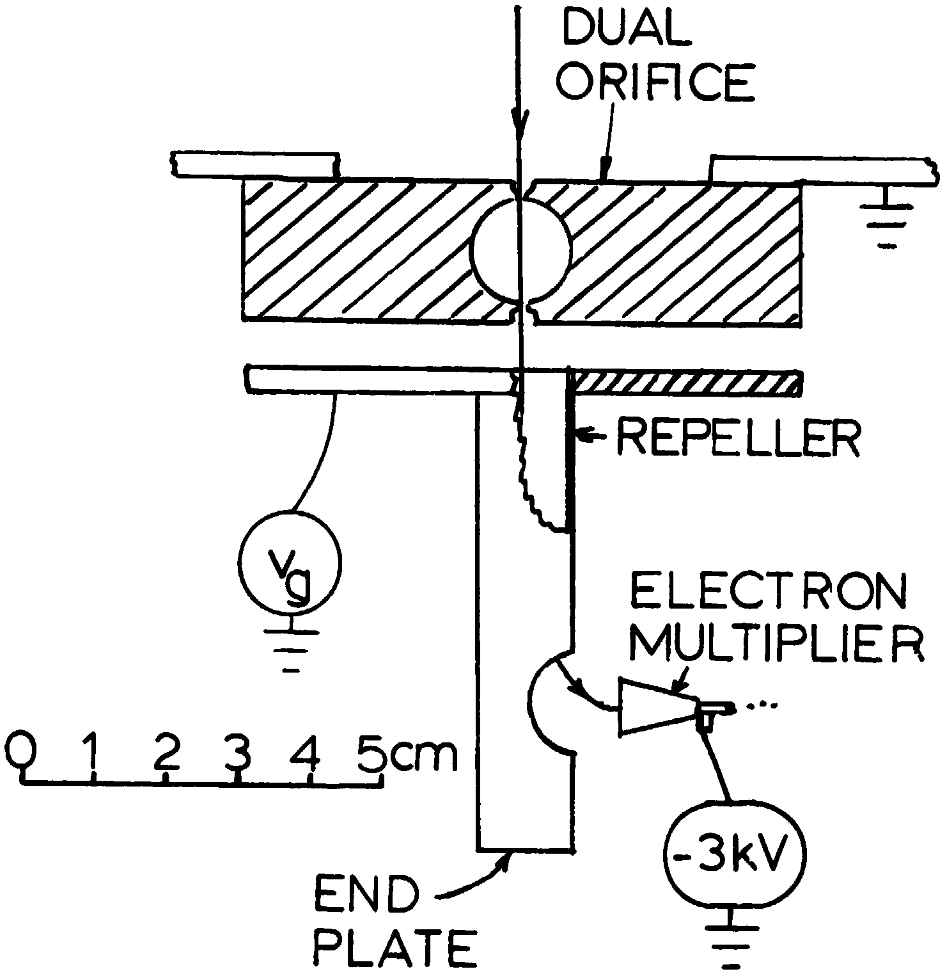

Fig. 12. Diagram of a prototype ion sensor showing an ion trajectory, orifices, repeller, and an ion detector which may be biased up to 3kV.

Two holes of 1-mm diam and separated by 12.7 mm defined the orifice area A and maximum angle of incidence or alternatively the parameter U, which was 0.0062. After ions passed through the orifices, they entered a drift tube maintained at potential v_g if their energy was sufficient. Otherwise they were collected on the back side of the orifice assembly. Ions passing down the drift tube were drawn out through a port to the negatively biased electron multiplier, each ion having a certain probability of producing an avalanche which could be counted. Note that low energy ions will have nearly equal trajectories and energies at the funnel so that they will have nearly equal detection efficiencies. The exception is for ions of high atomic mass which are of little interest for the intended application. Because of the geometry, the funnel will not intercept electrons streaming through the orifices nor will it attract them, though it may collect ions generated by electrons entering the instrument. Also the funnel is placed so as not to intercept photons entering the instrument. Vents in the case were shielded to prevent particles from entering other than through the intended orifices. Particles and photons passing through the drift tube were collected on the end plate though with some reflections occurring. A more carefully designed dump should ultimately be used.

The original instrument was fabricated with the two entrance holes erroneously misaligned by about one hole diameter. Measurements were taken with that configuration and then the outer hole was bored out and covered with an alignable diaphragm having the same hole diameter as before. Additional measurements were made for the new configuration (modification of Fig. 12) which had a hole separation S=15.9 mm and U=0.0040.

Test Sources

Two test sources could be mounted interchangeably with their apertures 30 cm above the face of the ion sensor. One was a commercial Lyman-α source producing an estimated 1.5×10^{10} photons $cm^{-2}s^{-1}$ at the face of the instrument. The other was a heated tungsten filament which could be biased negatively to produce electrons and positively to produce ions by contact ionization. The charged particle source, shown in Fig. 13, had a grounded cover and a focusing cup which was connected to the more negative side of the filament. The spread of particle energies from the source depended upon the length of the hot tungsten wire and the associated potential drop along its length.

The ion source operated with ambient pressures from 10^{-6} to 4×10^{-5} torr when air was being leaked into the system. No attempt was made to measure what constituents were being ionized, but presumably predominant were O_2 and H_2O which had the lowest ionization potentials of the common constituents of air. The source would not function with helium which has a much higher ionization potential. The ion source was operated with bias

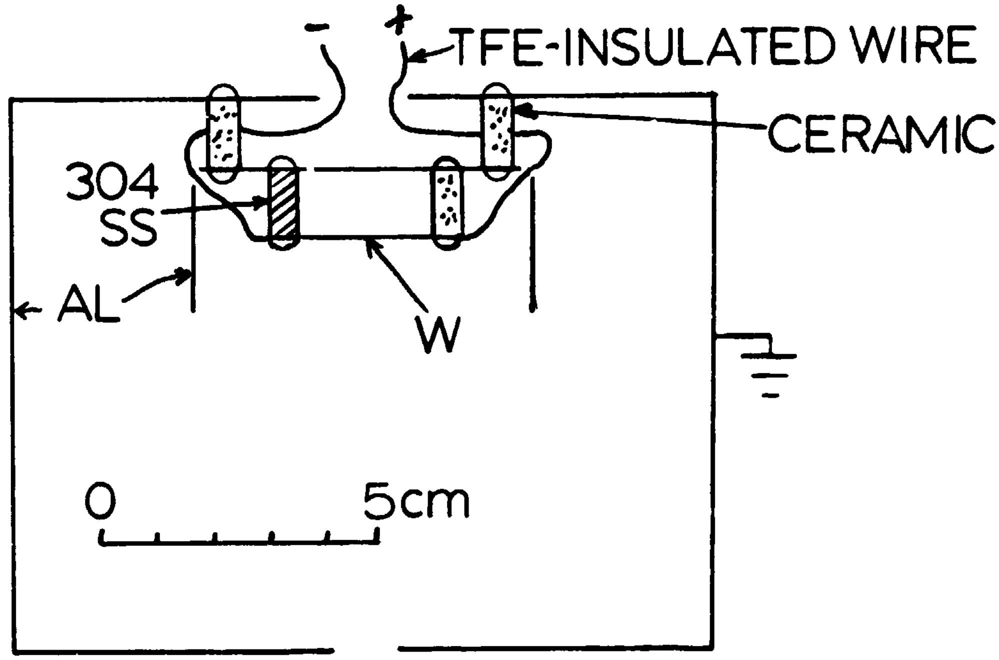

Fig. 13. Cross section of ion source.

voltages from 6 to 30 volts. Stable and consistent operation was obtained at the higher voltages and typical current density at the sensor was 10^{-13} A/cm^2.

Response to Ions

Measurements were made with ion beams having different energies, different energy spreads, and different angular orientations.

The response at normal incidence as a function of repeller voltage was measured for two ion beams having different accelerating potentials. Results are shown in Fig. 14 where the low counting rates are attributed to an assumed loss of source intensity when accelerating voltage is low. Figure 15 shows a steeper transition as well as the stronger signal associated with a source bias of 30 V. The ion energy spread depends however, not on the source bias, but on the length of the filament, which was reduced to 6 mm for the test shown in Fig. 15. This cutoff is characteristic of a

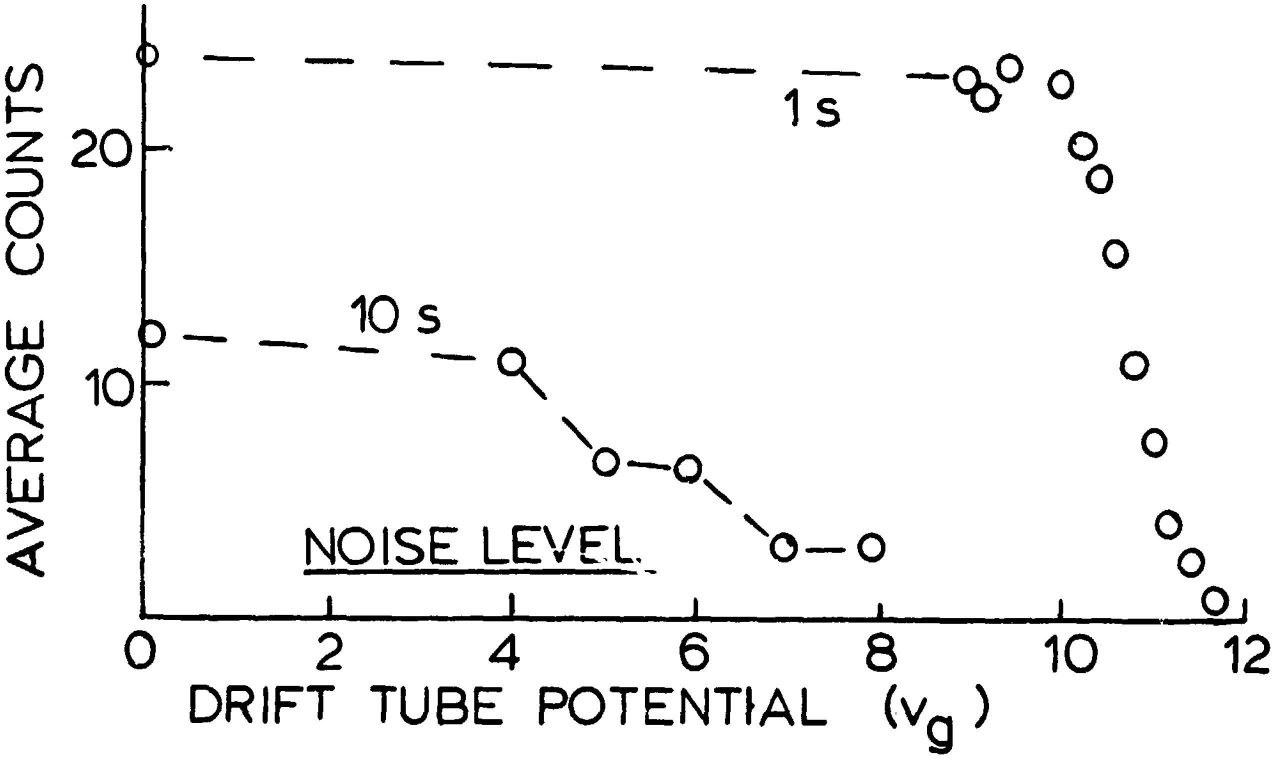

Fig. 14. Average counts for time periods shown when the ion source was at 5.9V and 10V.

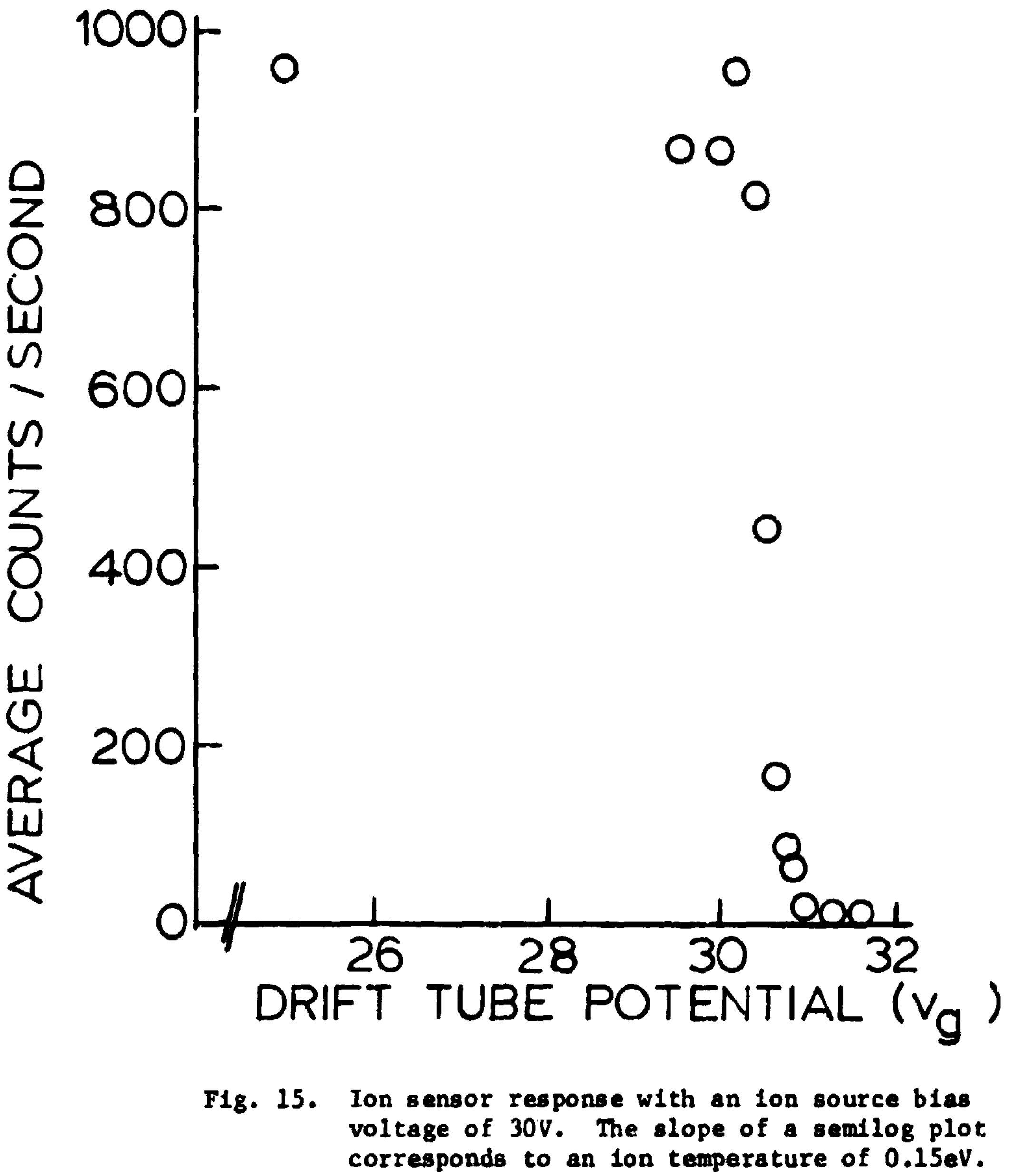

Fig. 15. Ion sensor response with an ion source bias voltage of 30V. The slope of a semilog plot corresponds to an ion temperature of 0.15eV.

Boltzmann factor, exp(-eV/kT), where T is 0.15eV. Consequently distributions such as those in Fig. 14 represent spreads in particle energy, not instrument response characteristics.

When the instrument is rotated, the response should vary according to the function shown in Fig. 8. Keeping only the linear portion one has

$$F = 1 - 4T/\pi \tag{61}$$

The graph in Fig. 16 compares the measured response with the straight line approximation for the original system with the misaligned holes. An asymmetrical response is noted. However, this distortion was eliminated by aligning the holes.

Another type of problem with the response is illustrated in Fig. 17 which is for the system with the holes aligned. Here the angle corresponding to peak response is found to be a function of repeller voltage, which ideally should not be the case. The explanation for this effect is presumably related to the asymmetric placement of the collection funnel. Though this asymmetry may be a problem for some types of measurement, it should not affect the response to isotropic sources such as the thermal plasma of interest.

Close examination of the data shown in Fig. 17 for a repeller voltage of 30.7 indicates still another type of distortion. The curve is redrawn in Fig. 18 to a different scale. The response on either side of the maximum is proportionally less relative to the peak than for the other cases.

Both of the previous problems are probably related to the nature of the potential contours in the drift tube. Ions must pass through a saddle point and ions with barely enough energy to pass may be reflected if they are not directed toward the optimum point. Thus ions entering at an angle will have a lesser probability of passing consistent with the data for 30.7 volts. Ions having energies considerably in excess of the minimum

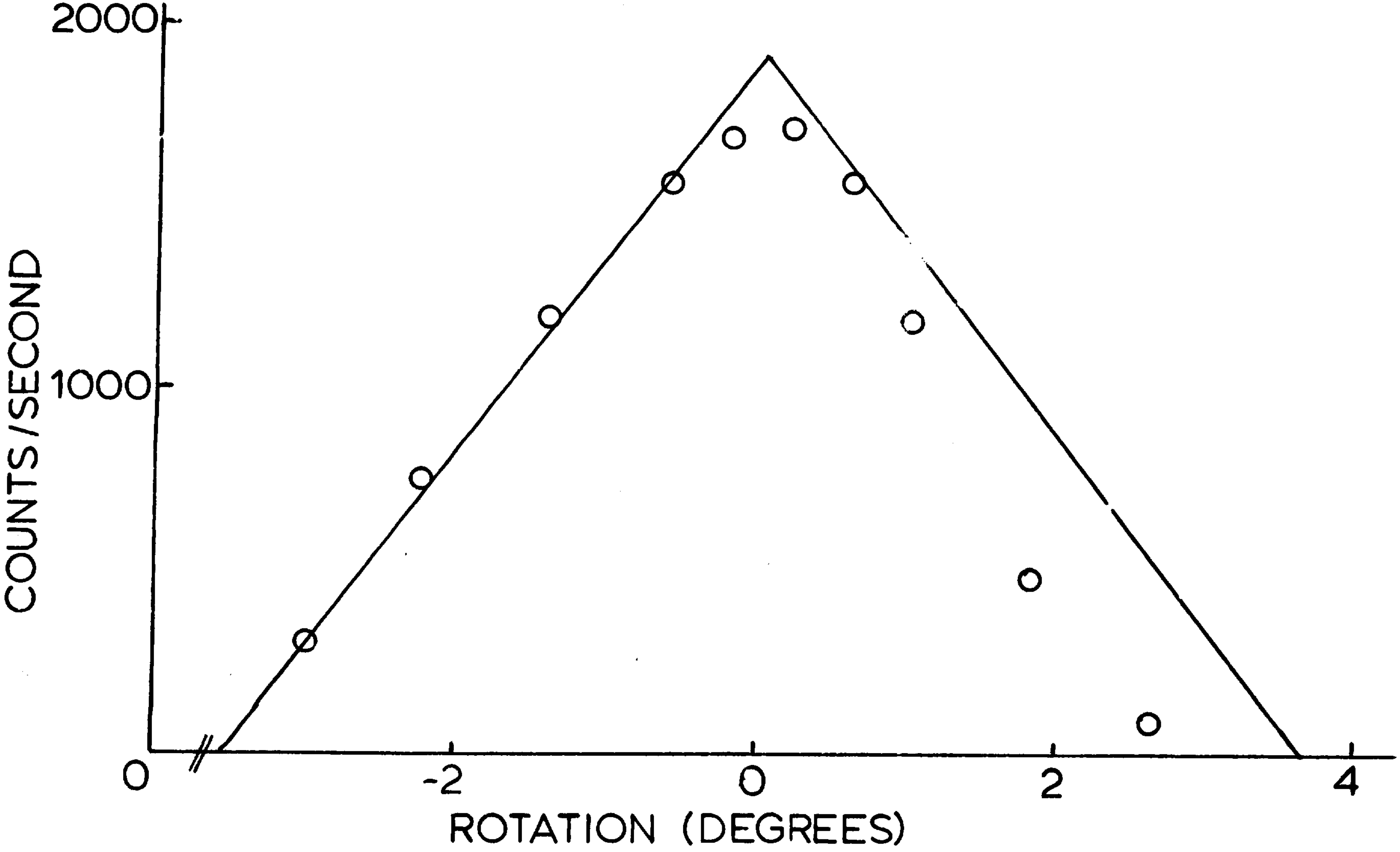

Fig. 16. Typical angular response of the system with misaligned holes. The straight lines represent Eq. 61.

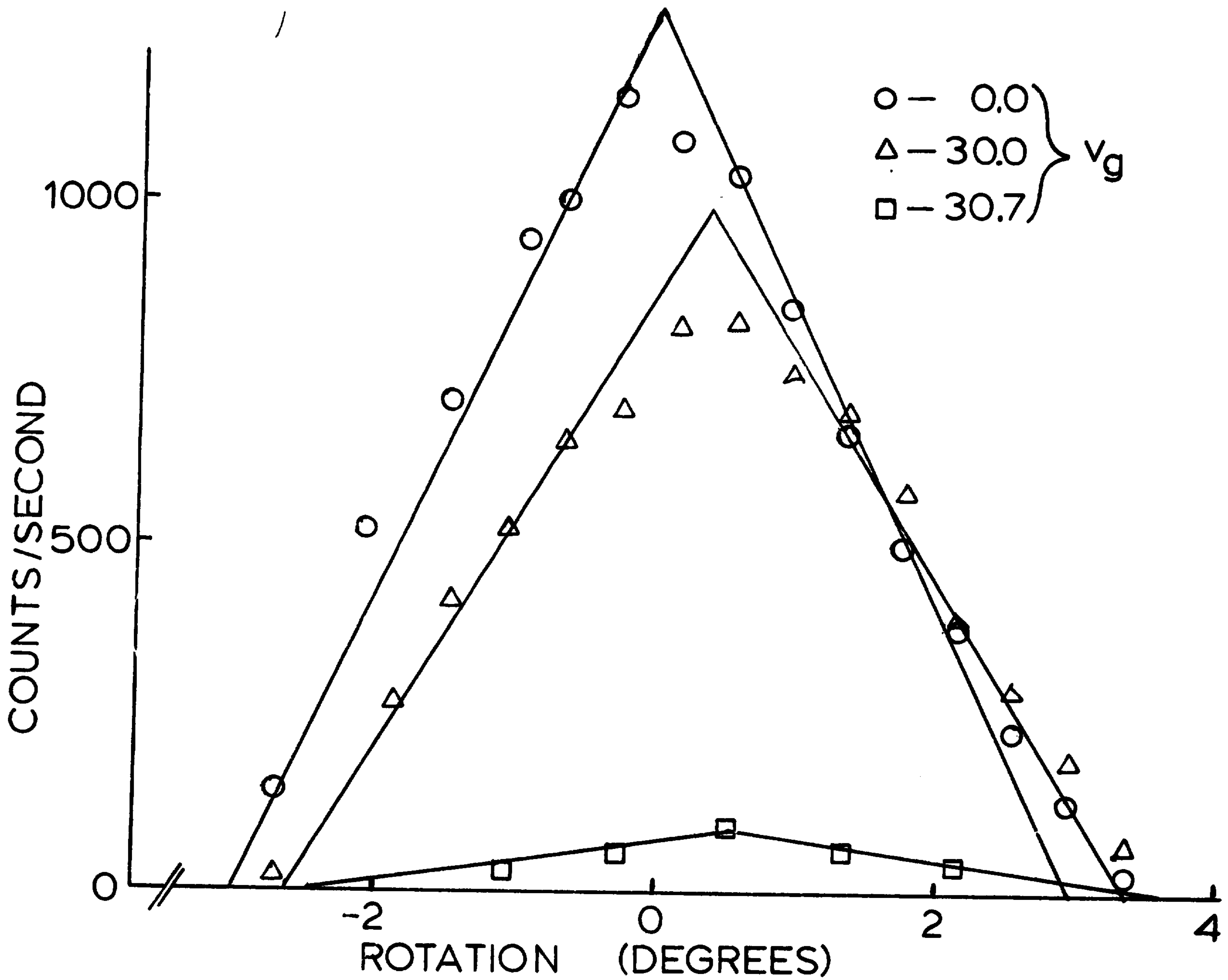

Fig. 17. Instrument response when the ion source is biased at 30V.

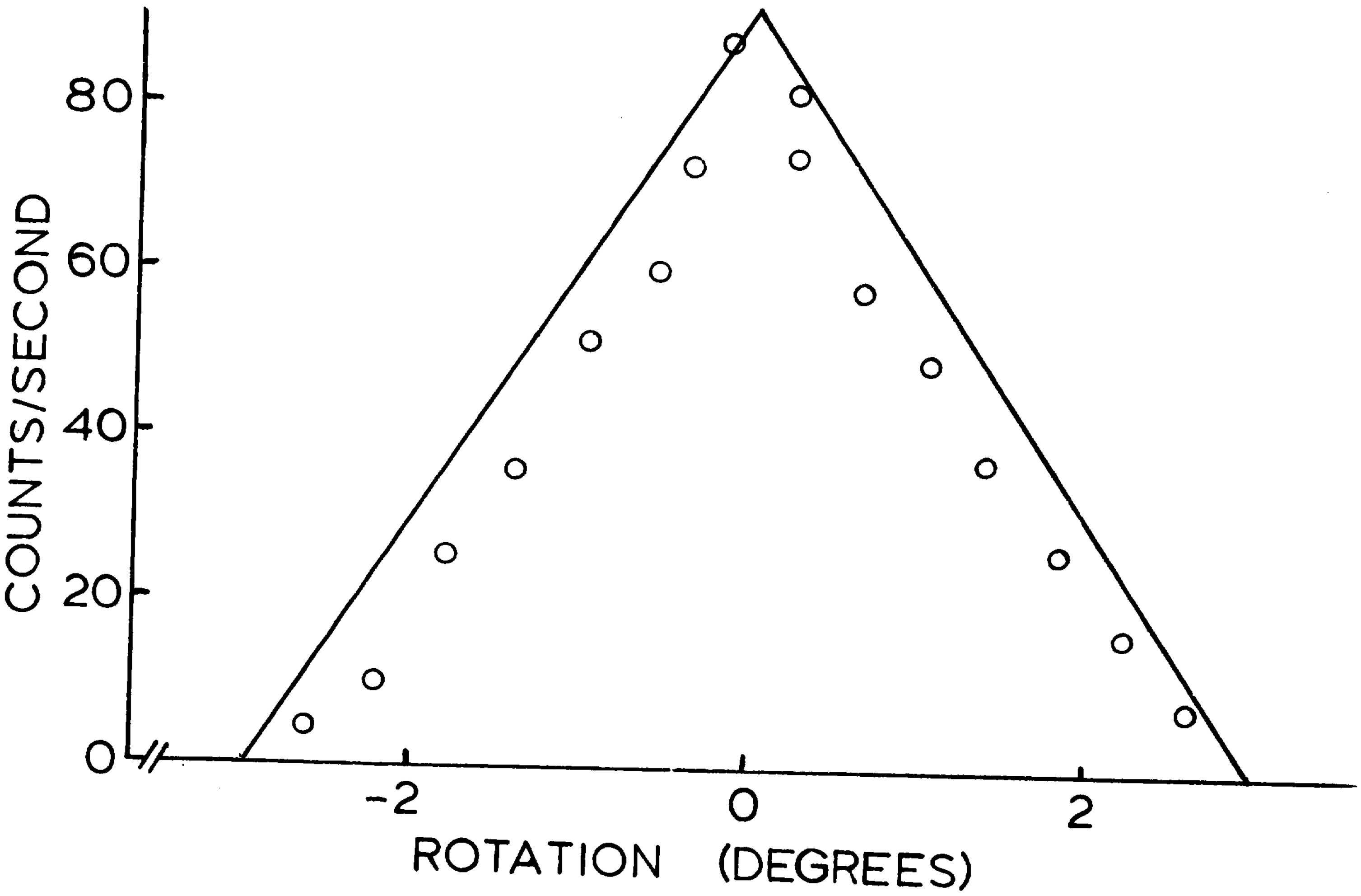

Fig. 18. Instrument response with v_g=30.7V when the ion source is biased at 30V.

will pass regardless of the exact nature of the saddle point as is the case for the data at 0 volts.

Response to Electrons and Photons

The response to electrons depends upon entering electrons producing ions by collision with background gas or the walls. The response is strongly dependent on cleanliness and it decreases with time. Also careful alignment reduces the response. No quantitatively valid data was recorded because of the variability of the response but counting rates eventually dropped below 1 Hz with the instrument facing the source.

The response to photons was high, with direct illumination giving rise to a count rate of 800 Hz. This is equivalent to approximately 5000 Hz in sunlight. However, the angle of response was limited to about ±5°. With care in designing the dump, one can reduce this rate considerably though how much is not known. The instrument was sensitive to leakage through the vents; counting rates of 5 Hz were obtained with the orifice covered. A small side lobe in the response occurred 14° off center when the entrance holes were misaligned.

Alternate Design

A different drift tube design has been described by Ross (Ref. 4) and it is illustrated in Fig. 19. After ions pass through the double apertures, they pass through a saddle-point potential which is controlled by the bias on the short drift tube between ground planes. The ions then exit from the chamber through a third aperture. Ross showed that if the third aperture is too small, the electrostatic focussing produced by the drift tube causes anomolous response. The dashed line in Fig. 20 is that response which can be avoided by making the aperture large enough. For this system the energy of particles which can pass through the saddle point

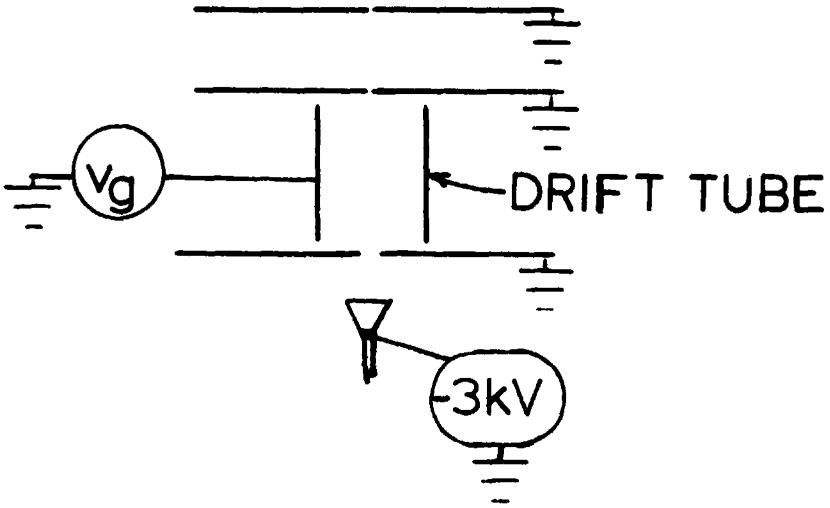

Fig. 19. Schematic of an alternate drift tube design.

is some fraction of the potential applied to the tube, that fraction being specified in Table 5.

TABLE 5

Ratio of Drift-Tube Radius to Length	Ratio of Saddle-Point Potential to Applied Potential
∞	π^{-2}
2.0	0.146
1.0	0.232
0.5	0.721
0.25	0.974
0.20	0.992

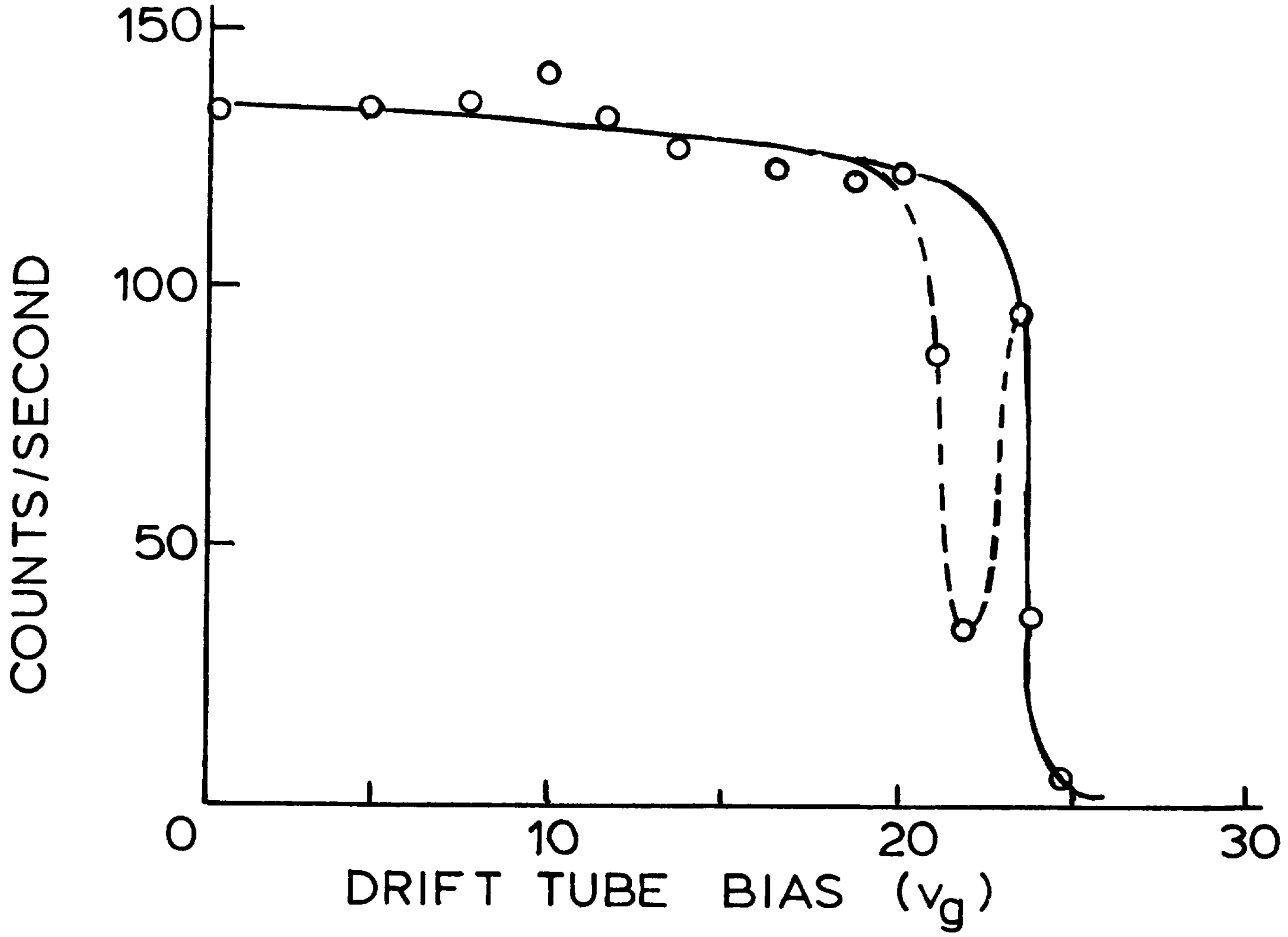

Fig. 20. Normal and anomalous response when the ion source is biased at 19.3eV and the ratio of radius to length is 0.45.

CONCLUSION

An instrument for measuring temperature and density of thermal ions above the plasma pause has been designed, built, and lab-tested, as detailed in the preceding chapters of this report. The design is an application of the general theory for ion measurements in the presence of sheaths and Mach effects [Ref. 1]. The predominating feature of the design is that particles having large angles of incidence are excluded; in practice the angle is limited typically to 4°. As a consequence of this feature, sheath size has little significance and theoretical approximations yield relatively simple expressions for instrument response. When prototypes were tested with monoenergetic sources, various abnormalities were identified and associated with design flaws for which corrective procedures are prescribed.

Results of the theoretical development are summarized by Eqs. 1, 36, 39, 42, and 43 which yield I, the current being measured, as a function of the many different parameters which may influence it. Table 2 provides the coefficients A_i used in these equations. Seldom is it necessary to use this full set of equations. Eqs. 58, 59, and 60 together represent a simplified set of equations which yield I in closed form and in terms of the parameters B, M, V_s, V, U, J_o and A. Typical error bars are given in Table 4.

Because the angle of incidence is limited, the energy discrimination process is easy to implement. A simple biased drift tube provides resolution as low as 0.15eV as illustrated by the data in Fig. 15. In fact the energy spread associated with potential drop along the source filament is easily noted in Fig. 14.

The theoretically predicted angular response function in the shape of the triangle was observed in numerous tests. Various minor anomolies in that shape can be attributed to design features which may be optimized. A saddle-point discriminator originally described by Ross [Ref. 4] isolates that region from the collection region such that the designer would have more control over the anomolies.

APPENDIX I

SOURCES OF ERROR IN THE USE OF FARADAY CUPS

These devices, known as traps, Faraday cups or retarding potential analyzers, have been used extensively both above and below the plasma pause, but the results have often been found to be in error, in retrospect. Cures are known for most of the problems, but the construction and interpretation of a fully debugged device is a major task.

The device generally consists of a collector plate separated from the plasma by numerous biased grids. It is flush mounted on the surface of the spacecraft. Current to the collector is monitored with an electrometer as a sequence of programmed voltages is applied to the grids.

Problems arising in the use of these types of instruments are itemized below. However, some of these are applicable to other kinds of particle detectors as well.

1. Internal photoemission. When sunlight strikes the collector, it produces photoelectrons which can be returned to the collector by a suppressor grid. However, reflected or oblique light strikes the back side of the suppressor and photoelectrons emitted there are attracted to the collector. Thus a spurious response occurs. Serbu and Maier (Ref. 5) ignored the data which was taken when their trap faced the sun (within 70°). Bridge et al. (Ref. 6) modulated their particle beam with a driven grid so that the desired current could be separated from the steady photocurrent with a tuned amplifier.
2. Photoemission and secondary emission from the spacecraft. These electrons are extremely difficult to distinguish from natural electrons, especially with a cup. They are not very important

at low altitudes where natural densities exceed, say, 10^3 cm^{-3}, but they are dominant above the plasma pause. Rosenbauer (Ref. 7) considers a method of separating the two types of electrons with a curved plate analyzer.

3. Secondary emission from suppressor grid and collector. The suppressor inhibits loss of secondaries from the collector, but it produces its own secondaries when struck by the incoming beam. Most of these will migrate outward and in any case, their significance can be kept low if the suppressor is highly transparent.
4. Secondary emission from walls of cup. This can be minimized by careful design.
5. Ion impact on retarding grid. When electrons are being collected, ions may impact on the retarding grid so as to produce secondaries which are attracted to the collector. This problem occurs only below the plasma pause, and it may be eliminated by proper design. Knudsen and Harris (Ref. 8) and Binsack (Ref. 9) have described the effects. Binsack used it as a plasma pause detector.
6. Grid wire spacing. Temperature calculations should be corrected to account for the error in assuming that a grid is equivalent to an equipotential plane. Hansen (Ref. 10) describes the correction.
7. B Fields. These are generally ignored and with justification though Wrenn and Heikkila (Ref. 11) have studied the effects on photoelectrons at low altitudes.
8. Ion species. If different types of ions are present (0+, He+, H+ at low altitude) then special computations are necessary (Ref. 12). See also item 9 which is related to this effect.

9. Mach effects and wakes. These are important especially at low altitude where ion temperature is low, average ion mass is high, and spacecraft velocity is high. Above the plasma pause, hydrogen ion velocities at 1 keV are comfortably in excess of spacecraft velocity but problems still occur for low energy ions. Whipple et al. (Ref. 1) include this effect in their theory. Sagalyn and Smiddy (Ref. 13) treat the problem as do Serbu and Maier (Ref. 5).

10. Aperture and acceptance cone. These depend on grid transparency, grid spacing, particle type (possibly), and particle energy. They can be measured and/or calculated. See Bonetti et. al. (Ref. 14).

11. Backscatter. Electrons approaching the collector may backscatter with sufficient energy to escape. The fraction is typically from 10 to 30%, and it is larger for high Z metals (Ref. 15).

12. Potential and sheath effects. The response of a trap depends on spacecraft potential and sheath size. These effects may be treated by iterating to a solution with potential and sheath thickness as parameters. The calculations developed by Whipple et al. (Ref. 1) involve numerical quadratures. The effects disappear when potential goes to zero, when temperature becomes large, or when sheath size goes to zero.

13. When thermal densities are low, the signal associated with thermal ions may be obscured by the constant current associated with the high energy flux.

14. The sensor must be mounted and spacecraft attitude controlled so that the bearing of the trap does not change during the settling time . Otherwise data taken in directional plasma flows may be

averaged in an unpredictable manner. The ability to reorient the trap is desirable.

15. Conducting surfaces should have uniform work functions if low energy measurements are to be accurate. Gold plating and carbon have been used to achieve uniformity.

REFERENCES

1. Whipple, E. C., Warnock, J. M., and Winkler, R. H.: "Effect of Satellite Potential on Direct Ion Density Measurements Through the Plasmapause," J. Geophys. Res. 79(1), pp. 179-186, January 1974.

2. Harris, K. K.: "The Measurement of Cold Ion Densities in the Plasma Trough," J. Geophys. Res. 79(31), p. 4654, November 1974.

3. Chappell, C. R.: "Detached Plasma Regions in the Magnetosphere," J. Geophys. Res. 79(13), p. 1861, May 1974.

4. Ross, D. P.: "Ion Tracking in an Electrostatic Potential Distribution," The Pennsylvania State University, NASA-CR-156983, May 1978.

5. Serbu, G. P., and Maier, E. J. R.: "Observations from OGO 5 of the Thermal Ion Density and Temperature Within the Magnetosphere," J. Geophys. Res. 75(31), pp. 6102-6113, November 1970.

6. Bridge, H. S., Dilworth, C, Rossi, B., and Scherb, F.: "An instrument for the Investigation of Interplanetary Plasma," J. Geophys. Res. 65(10), pp. 3053-3055, October 1960.

7. Rosenbauer, H. R.: "Possible Effects of Photoelectron Emission on a Low Energy Electron Experiment."

8. Knudsen, W. C., and Harris K. K.: "Ion-Impact-Produced Secondary Electron Emission and Its Effect on Sapce Instrumentation," J. Geophys. Res. 78, p. 1145, March 1973.

9. Binsack, J. H.: "Plasmapause Observations with the M.I.T. Experiment on IMP2," J. Geophys. Res. 72(21), p. 5231, November 1967.

10. Hanson, W. B., Frame, D. R., and Midgely, J. E.: "Errors in Retarding Potential Analyzers Caused by Nonuniformity of the Grid Plane Potential J. Geophys. Res. 77(10), pp. 1914-1922, April 1972.

11. Wrenn, G. L., and Heikkila, W. J.: "Photoelectrons Emitted from ISIS Spacecraft."

12. Knudsen, W. C.: "Evaluation and Demonstration of the Use of Retarding Potential Analyzers for Measuring Several Ionsopheric Quantities," J. Geophys. Res. 71(19), pp. 4669-4678, October 1966.

13. Sagalyn, R. C., and Smiddly, M.: "Charged Particle Measurement by Means of Electrostatic Probes," AFCRL-69-0426, N70-21470, October 1969.

14. Bonetti, A., Bridge, H. S., Lazarus, A. J., Rossi, B., and Scherb, F. S.: "Explorer 10 Plasma Measurements," J. Geophys. Res. 68(13), p. 4017, July 1963.

15. Sternglass, E. J.: "Backscattering of Kilovolt Electrons from Solids," Phys. Rev. 95(2), pp. 351-353, July 1954.

ACKNOWLEDGEMENTS

The author appreciates the encouragement and assistance of N. John Stevens and others at the NASA-Lewis Research Center where he completed portions of this work as a NASA-ASEE fellow.